X-RAY PULSAR NAVIGATION INSTRUMENT PERFORMANCE AND SCALE ANALYSIS

A Thesis
Presented to
The Academic Faculty

by

Jacob Hurrell Payne

In Partial Fulfillment
of the Requirements for the Degree
Master of Science in the
Daniel Guggenheim School of Aerospace Engineering

Georgia Institute of Technology
December 2019

X-RAY PULSAR NAVIGATION INSTRUMENT PERFORMANCE AND SCALE ANALYSIS

Approved by:

Dr. E. Glenn Lightsey Advisor
School of Aerospace Engineering
Georgia Institute of Technology

Dr. Brian Gunter
School of Aerospace Engineering
Georgia Institute of Technology

Dr. David Ballantyne
School of Physics
Georgia Institute of Technology

Date Approved: December 5, 2019

ACKNOWLEDGEMENTS

This research has made use of data, software and web tools obtained from NASA's High Energy Astrophysics Science Archive Research Center (HEASARC), a service of Goddard Space Flight Center and the Smithsonian Astrophysical Observatory.

I would like to thank all the researchers whose work this builds upon. I started this project with limited knowledge of pulsars or x-ray physics and the detailed papers presented as references here are greatly appreciated. My thanks goes to Dr. Suneel Sheikh in particular for providing an understanding of the field and answering my questions about his work.

I would like to especially thank Dr. Glenn Lightsey, Dr. Brian Gunter and Dr. David Ballantyne for their insight and support throughout this project. It is certainly no overstatement that this would not have been possible without their contributions.

TABLE OF CONTENTS

LIST OF TABLES

LIST OF FIGURES

LIST OF SYMBOLS AND ABBREVIATIONS

ARGOS	Advanced Research and Global Observation Satellite
AXAF	Advanced X-ray Astrophysics Facility, now Chandra X-ray Observatory
CRL	Compound Refractive Lens
DoP	Dilution of Precision
DSN	Deep Space Network
FWHM	Full Width, Half Maximum
HEASARC	High Energy Astrophysics Science Archive Research Center
keV	Kilo Electronvolt
MPL	Multiple Prism Lens
NICER	the Neutron star Interior Composition ExploreR
NuSTAR	Nuclear Spectroscopic Telescope Array
PMMA	Poly(methyl methacrylate)
RSS	Root sum squared
SDD	Silicon Drift Detector
SEXTANT	the Station Explorer for X-ray Timing and Navigation Technology
SLS	The Space Launch System rocket
SNR	Signal to Noise Ratio
SNR	(not used here) in some references, Super Nova Remnant
SPL	Stacked Prism Lens
ToA	Time of Arrival
XRC	X-Ray Concentrator

SUMMARY

This thesis investigates instruments for autonomous satellite navigation using measurements of X-ray emissions from millisecond pulsars. A manifestation of an instrument for this purpose, called the Neutron star Interior Composition Explorer (NICER), was launched to the International Space Station in 2017. The NICER instrument was designed to observe X-ray emissions from neutron stars for astrophysics research, and is out of scale in terms of volume, power consumption, mass and mechanical complexity to be useful for small satellite missions. This work surveys the range of existing X-ray observation missions to tabulate collecting areas, focal lengths, and optical configurations from milestone missions which describe the evolution of the state of the art in X-ray observatories.

A navigation demonstration experiment, called the Station Explorer for X-ray Timing and Navigation Technology (SEXTANT), was conducted using the NICER instrument. The experimental performance observed from NICER through the SEXTANT navigation demonstration is compared to theoretical predictions established by existing formulations. It is concluded that SEXTANT benefits from soft band (0.3-4 keV) exposure to achieve better accuracy than predicted by theoretical lower bounds.

Additionally, investigation is presented on the readiness of a navigation instrument for small satellites using compound refractive lensing (CRL) and derived designs. X-ray refraction achieves a much shorter focal length than grazing incidence optics at the expense of signal attenuation in the lens material. Performance estimates and previous experimental results are presented as a baseline for physical prototypes and

hardware testing to support future development of a physical instrument. The technological hurdle that will enable this tool is manufacturing precise lenses on a 3-micron scale from materials like beryllium with low atomic mass. Recent X-ray concentrator concepts demonstrate progress towards an implementation that can support a CubeSat scale navigation instrument optimized for soft band (0.3-4 keV) X-rays.

CHAPTER 1. INTRODUCTION

Since pulsars were first observed in 1967, researchers have considered these unique stellar objects for navigation. [1] In the most public example, the golden records on the Voyager probes included diagrams of Earth's position within the Milky Way, designated relative to pulsars. In the present day, new observations allow us to validate proposed navigation methods for real-time onboard spacecraft. Specifically, this work seeks to validate previously derived theory describing achievable accuracy of pulsar navigation by comparing the predicted range-estimate error with the experimental error from new instruments.

This navigation strategy offers a potentially robust way to provide autonomous navigation measurements for deep space missions. All interplanetary missions to date have been successful without such an instrument, so this research will present the role this new navigation technology could fill, informed by calculations of expected performance. A range of existing space-based X-ray observatories is presented to document the design space of current instrument capabilities. The intent is to identify trends of performance metrics relative to volume required to support this device, namely detector area and focal length. This analysis demonstrates the feasibility of a scaled instrument design for a "3U" CubeSat frame. A CubeSat "U" is one 10 x 10 x 10 cm cube, which is commonly patterned into a 10 x 10 x 30 cm frame called a 3U to allow more volume for scientific instruments alongside attitude control sensors and actuators.

1.1 Motivation

This work is inspired by recent developments in X-ray navigation. The Neutron Star Interior Composition ExploreR (NICER) instrument was designed to look at the very faint X-ray signals emitted by neutron stars. It was launched to the International Space Station in 2017 to study the equation of state for neutron stars, describing the composition and dynamics of these extremely dense objects and neighboring structures like companion stars and accretion disks. [2] The NICER instrument provided measurements for a pulsar navigation experiment in 2017, and results were published in 2018 showing the first on-orbit position estimation using pulsars. [3] The Station Explorer for Timing And Navigation Technology (SEXTANT) project successfully demonstrated a real-time navigation solution with accuracy better than 10 km, worst direction (i.e. $\sqrt{10^2 + 10^2 + 10^2} = 17.3$ km RSS).

The results published by the SEXTANT team present the accuracy of novel X-ray navigation measurements by the difference to GPS solutions, used as truth. Here, comparison is given between the SEXTANT navigation solution and a theoretical lower bound on navigation accuracy. The publication by Sheikh, et al., describing the theoretical bound presents comparison with experimental measurements from the Unconventional Stellar Aspect instrument on board the Advanced Research and Global Observation Satellite (ARGOS) spacecraft, which made timing measurements of millisecond pulsars in 1999 but did not include a real-time navigation experiment or accurate true position knowledge.[37]

Navigation Autonomy

A continuous navigation solution is useful for all missions and required for the majority to maintain accurate data position registration from scientific instruments and successfully perform orbital maneuvers. Since state propagation quickly loses accuracy without periodic measurement updates, an external, absolute measurement must be leveraged to eliminate drift.

The need for navigation autonomy will increase as more multi-actor, long-range missions are deployed. It is difficult for operators to communicate frequently with each craft in a constellation individually, especially for deep space missions where high-power or sensitive equipment is needed. The schedule for data relay and radio ranging time on the Deep Space Network will become strained as the number of spacecraft in need of command and telemetry increases.[4] Therefore, an autonomous navigation instrument which relies on natural phenomena instead of human-built infrastructure would alleviate a potential concern for deep space missions.

Small satellites are gaining popularity across many mission architectures as flight heritage grows and launch services become more accessible. Space flight is incrementally modernizing by adopting standard practices and form factors, with the Cal Poly CubeSat Design Specification at the forefront.[5] Small satellites now support missions beyond low Earth orbit with the first interplanetary CubeSats, MarCO 1 and 2, which flew with the Mars Insight lander and the upcoming deployment of thirteen CubeSats on the first launch of NASA's Space Launch System (SLS) rocket, Artemis-1.[4] Small satellites can ideally provide many benefits over traditional spacecraft by reducing the resources

required for any particular flight unit and therefore reducing the programmatic risk of losing individual satellites. This fact encourages missions which deploy constellations of small satellites for collaborative efforts in space exploration.

Pulsar navigation relieves reliance on Earth and other infrastructure. As the number of missions beyond low Earth orbit is increased, the need for autonomous navigation is amplified. In particular, the Deep Space Network (DSN) is a limited resource for navigation and is nearing capacity with a schedule to increase from 33 to 48 supported spacecraft in the next three years [6]. DSN is an incredible resource but creates a choke point for missions beyond Earth and Lunar space. This tension highlights the benefits of autonomous navigation; reducing reliance on external infrastructure allows more missions to operate simultaneously.

Using Earth-based infrastructure also has implications of diminishing precision as distance from Earth increases. Autonomous navigation provides more uniform accuracy throughout the solar system. Even still, the proposed Delta-correction pulsar navigation scheme, discussed in 3.1, relies on a catalog which is currently produced on Earth and causes performance to degrade with distance relative to the solar system barycenter. Distributing X-ray observatories with high timing accuracy on all interplanetary missions will provide autonomous navigation while simultaneously improving the accuracy of the scheme for all spacecraft subscribed to a jointly updated catalog of absolute pulsar timing.

1.2 Research Contributions

1.2.1 Experimental Validation of Theoretical Error Lower Bound

Previously formulated error analysis is compared to the flight data from the SEXTANT demonstration to provide experimental support and highlight discrepancies. The signal to noise ratio presented by Sheikh is used to produce an expected lower bound to position accuracy.[15] This formulation, described in detail in Chapter 3, takes several properties of the target pulsars, the background radiation and the observation instrument into account to estimate a variation of signal arrival certainty. Since photon time of arrival is used as the navigation measurement, variance in photon time of arrival is transformed into range accuracy.

The SEXTANT team published their range accuracies as well as the timing of observed targets.[3] From this information, a time series of expected accuracies is produced. Since line of sight to the observed pulsars is known, a three-dimensional dilution of precision can be calculated and compared to the 3D error produced by the NICER team. This analysis is conducted, and the experimental RSS error is noted to be significantly lower than the theoretical lower bound. SEXTANT uses a state-estimate filter and a softer energy band to achieve gains that are not accounted for in the SNR formulation. Navigation instruments should be sensitive to the soft X-ray band to achieve the best accuracy, which is better than the previous theoretical predictions.

1.2.2 Investigation of Novel Optics Configurations

Radio observations have been the most common method of detecting pulsars since radio signals are only slightly attenuated by the atmosphere, unlike X-rays which experience photo-electric absorption. However, the large, sensitive radio receivers that can be constructed on the ground are not applicable to spacecraft for navigation. Instead, X-ray emissions from pulsars are observed with instruments that have geometric collecting areas on the order of one meter in diameter or smaller. The soft X-ray emissions are relatively bright, with pulse profiles that are very stable in time.

Recent research in X-ray optics has demonstrated fabrication of Compound Refractive Lenses (CRL) for X-rays [7] which achieve focal lengths less than 30 cm [8] and can be accommodated by common 3U or 6U CubeSat structures. The new lensing technique has not been applied to two-dimensional concentrating arrays for scales larger than one square centimeter. CRL configurations are also not typically sensitive in the energy band recommended by the investigation from the first contribution.

A study from September 2019 demonstrates a novel adaptation of CRL styled X-ray lensing called Stacked Prism Lensing, but only tested for performance with hard X-rays of 10 keV or more.[32] This instrument achieves better effective area and lower material attenuation for soft X-rays than previous optics. A baseline survey of existing capabilities is established and an SPL configuration for a CubeSat is presented.

CHAPTER 2. TRADE SPACE OF SOFT X-RAY INSTRUMENTS

The preliminary portion of this research involved studying existing X-ray observatories to understand and document the design space. To this end, the NASA High Energy Astrophysics Science Archive Research Center (HEASARC) provided by the Goddard Space Flight Center has proven an invaluable resource.[34] Observation data is available directly from eleven active missions, with detailed documentation for twenty-eight past missions and references for a total of 103 studies in high-energy astrophysics. A subset of these have proven key players in observing astronomical X-ray sources. This chapter starts with the introduction of some terminology, then discusses the type and scale of some 'milestone' observatories.

The field of high-energy astronomy has its own lore and language which is useful to understand. This chapter uses the conventions of the field to discuss the area of detectors and styles of X-ray concentrating optics. Across professions dealing with X-rays, radiation is described in units of energy rather than frequency or wavelength. The conversion uses Planck's constant, h, and the speed of light, c, to describe the energy carried by individual photons based on wavelength, λ.

$$E = \frac{hc}{\lambda} \tag{1}$$

X-rays are loosely branched into two categories, based on energy levels measured in electron-Volts. Soft X-rays cover the electromagnetic spectrum from the end of high-energy ultraviolet to five or ten kilo electron-volts (keV). In terrestrial practicality, soft

X-rays may not even be classified as X-rays since their energy is relatively low, although still high enough to cause ionization. The Georgia Tech Office of Radiological Safety considers any source that emits above 5 keV to warrant precautions. [9] Hard X-rays span from there up to Gamma rays, and typically range from 30 to 100 keV.

The observed flux from cosmic X-ray sources is very faint; described using centimeter-gram-second (cgs) units, flux values are typically 9 to 13 orders of magnitude below one $\left(10^{-9} \text{ to } 10^{-13}\ \frac{\text{ergs}}{\text{cm}^2 s}\right)$. An erg is one tenth of a micro-Joule, or 1 erg $=$ $1\ \text{J} \times 10^{-7}$. The effective area used to calculate the total energy imparted on the detector is reduced from the geometric exposure area. Effective area is the product of reflectance and geometric area, and so is affected by material properties of reflective surfaces and parameters of the geometric configuration.[10] Reflectance, R, is determined by the complex index of refraction for material j, $n_j = n_{rj} - ik_j$, as used in equation 2 for light traveling from material 1 to material 2. The real part of the index $n_r = 1-\delta$ is greater than one for visible light, which causes visible light to focus through convex lenses. The opposite is true for X-rays, where the decrement δ of the real refractive index is $0 < \delta \ll 1$. The imaginary part of the index describes attenuation of the signal and causes R to be less than one for the extinction coefficient $k > 0$, resulting in energy losses. If $k = 0$, light continues without loss.

$$R = \frac{(n_{r1} - n_{r2})^2 + (k_1 - k_2)^2}{(n_{r1} + n_{r2})^2 + (k_1 + k_2)^2} \tag{2}$$

Since reflectance – and therefore effective area – depend on the energy of the incident radiation, a continuous function of spectral effective area could be calculated for

the full band of received energies; the variation of effective area is significant. In Figure 1, the maximum effective areas are plotted against launch year for the observatories identified in Table 1. These observatories are all capable of detecting soft X-ray sources and the maximum effective areas are taken at 1 to 3 keV.

There is a weak trend upward in effective area shown for the observatories that have successfully been launched. The slowed growth of effective area over the last three decades is likely due to stagnation in launch vehicle payload capacity. This trend is disrupted significantly by XPNAV-1 [28] and the CubeX proposal [14] showing modern interest in applications for X-ray detectors outside astronomy and leading to the divergence of small satellites from larger telescopes like NICER and STROBE-X [13], a satellite proposal with scaled NICER hardware presenting more than 20,000 cm^2 effective area at 1.5 keV.[13] XPNAV-1 is a Chinese satellite launched in 2016 to observe X-rays emitted from pulsars as a study in small x-ray optics for navigation with a Wolter Type 1 telescope of 30 cm^2 effective area and 60 cm focal length, which is still too large for a 3U frame. CubeX is a mission concept using a concentrator similar to XPNAV-1 for a lunar surface study and navigation demonstration.

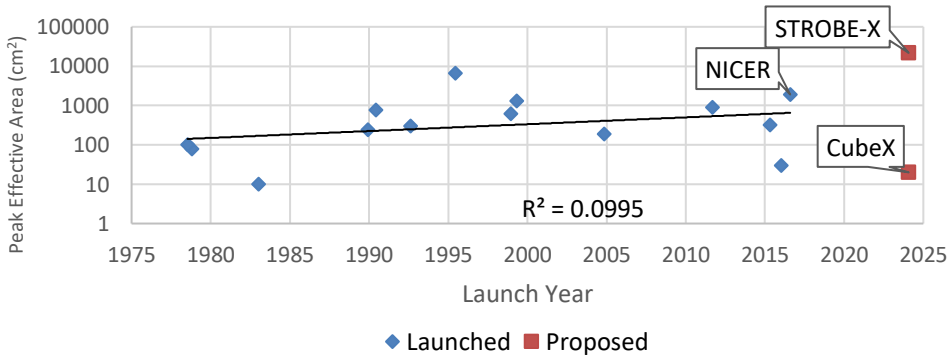

Figure 1 - Effective Area of X-ray Observatories by Launch Year

X-ray observations took many forms in their early years, starting from detectors on sounding rockets in the early sixties. [11] Throughout the evolution of detection equipment, there has been a strong desire in X-ray astronomy to increase the effective area of observatories. The counteracting force to building larger effective area is the expense and complication of launching large optical instruments to orbit. Since X-rays are attenuated by Earth's atmosphere, observations of X-ray emissions must take place off the ground. The X-ray emissions from distant sources are also very faint, less than 3 photons$/(\mathrm{cm}^2$ s) observed for all but the brightest sources. As such, the primary engineering challenge has been increasing the effective area presented to incoming high-energy particles and concentrating these photons onto a detector.

As a note on units and convention, flux from the Crab Nebula sets the standard for X-ray sources, to the extent that other sources are occasionally described in units of milliCrab and the nebula is used to calibrate new instruments. One Crab is 2.4×10^{-8} erg / (cm^2 s), or 3.3 photon counts per square centimeter per second in the 2-10 keV range.

The most common optical instrument for increasing effective area is the Wolter Type 1 telescope, shown in Figure 2. This device is two layers of nested concentric shells that reflect X-rays at very low angles of incidence. If higher angles of incidence are used, X-rays tend to refract straight through the shells and are not concentrated towards a detector. The theory behind Wolter Type 1 arrangements dictates using a parabolic reflective surface and then a hyperbolic surface to most efficiently concentrate incident radiation. In practice, replacing one set of shells with conical sections reduces complexity of fabrication and does not significantly reduce performance. Modern Wolter Type 1 concentrators aim to maximize the number of concentric shells to improve the gain.

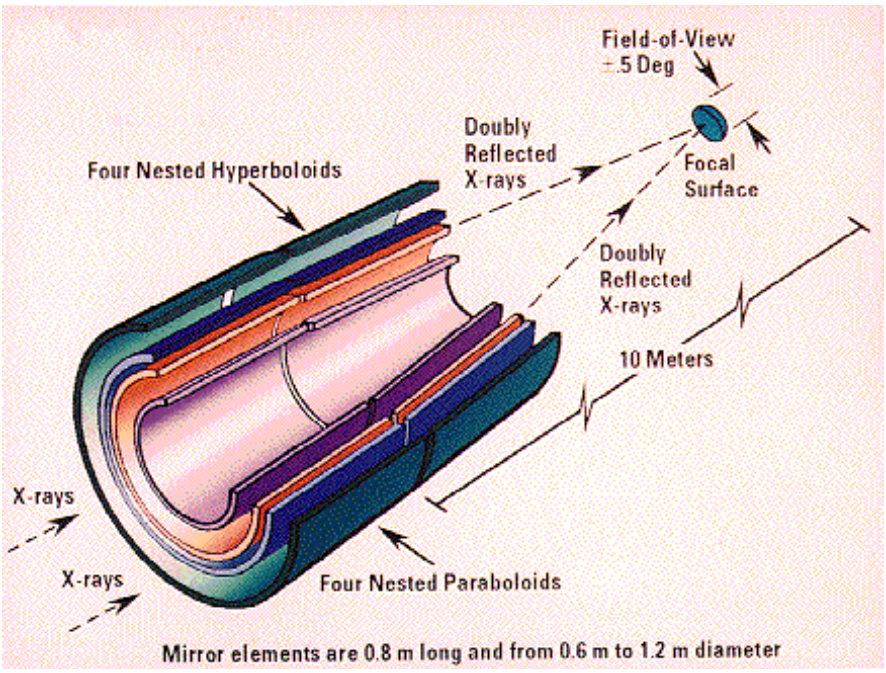

Figure 2 - Wolter Type 1 Telescope from Chandra (AXAF)[35]

Wolter Type 1 telescopes have a scalable but relatively static geometry. The optimal angle of incidence is set by the index of refraction, so overall shape remains similar with scale. As such, the focal length is determined by the geometric area of the concentrator area in roughly a 10:1 relationship. The drive to increase area has led to many missions flying with deployable masts or booms – most recently NuSTAR seen in Figure 3 – to spread the instrument bench apart from concentrating elements. The Hitomi mission successfully deployed an "Extendable Optical Bench" mechanism, but the spacecraft malfunctioned and broke apart less than three months after launch due to an attitude control error.[12] Longer focal lengths are feasible to launch on modern rockets with deployment mechanisms, but geometric collecting area is difficult to increase without some novel approach.

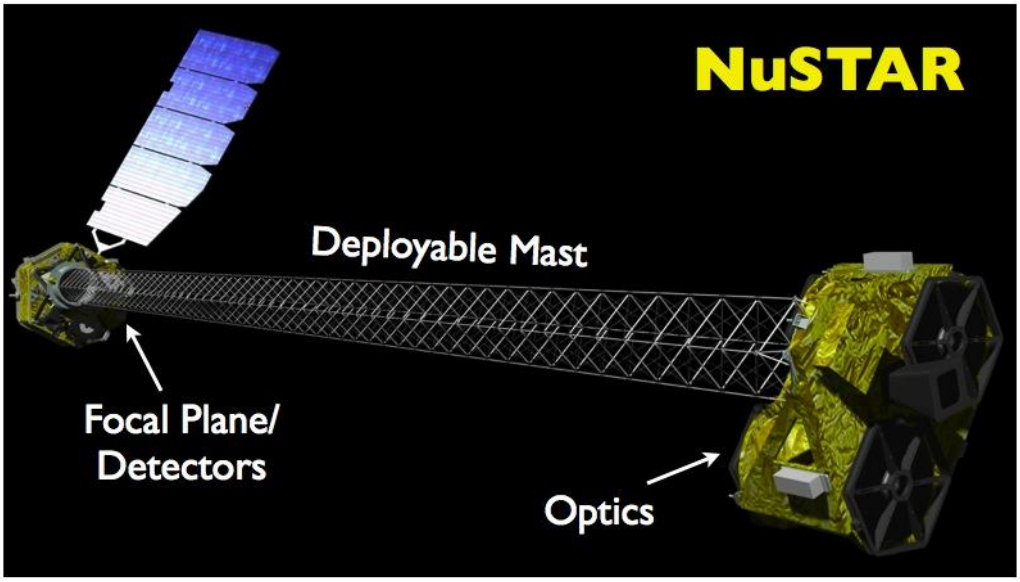

Figure 3 - The Nuclear Spectroscopic Telescope Array Mission (NuSTAR)[36]

Now that conventions of the field have been clarified, the data in Table 1 is presented to summarize the state of soft X-ray observatories by highlighting some milestone missions. This catalog draws from NASA's HEASARC observatory list with some additions. The performance metrics of interest for this research are focal length and collection area as the limiting dimension of instrument miniaturization. Energy bandwidth is required to include soft X-rays in the 0.1 to 4 keV range to detect known millisecond pulsars. Field of view and energy resolution are less impactful for navigation but are worth considering for dual-purpose instruments with scientific applications.

Table 1 - Comparison of Notable X-ray Observatories

Observatory	Launch Date	Detector	Energy Range (keV)	Max Effective Area (cm^2) [0.1-2.5 keV]	Focal Length (cm)	Optics
Chandra X-ray Observatory (AXAF)	1999-07-23	ACIS back	0.1-10	615	1000	Wolter Type 1
		ACIS front	0.4-10	525		
		HRC	0.1-10	215		
		HETG	0.6-10	45		
		LETG	0.1-6	105		
XMM-Newton (X-ray Multi-Mirror Mission)	1999-12-10	EPIC MOS	0.2-12	1180	750	Wolter Type 1
		EPIC PN	0.2-12	1304		
		RGS	0.4-2.5	185		
Hakucho (CORSA-B)	1979-02-21	VSX	0.1-0.2	78		N/A
		SFX	1.5-30	69		
		HDX	10-100	49		
Suzaku	2005-07-10	XRS	0.3-12	190	475	
		XIS	0.2-12	1600		
ASCA	1993-02-20	SIS	0.4-12	300	350	Wolter Type 1
		GIS	0.6-12	145		
ROSAT	1990-06-01	PSPC	0.1-2.4	240	240	Wolter Type 1
		HRI	0.1-2.4	80		
Einstein (HEAO-2)	1978-11-12	XRT	0.1-4	0	340	Wolter Type 1
		MPC	1.5-20	667		
Hitomi	2016-02-17	SXS	0.3-10	323	560	Wolter Type 1
RXTE	1995-12-30	PCA	2-60	700		Coded Aperture
NICER	2017-06-03	XTI	0.2-12	1900	108.5	1 Stage Grazing Incidence
EXOSAT	1983-05-26		0.05-50	0	110	Wolter Type 1
NuSTAR	2012-06-13		3-79	900	1014	Wolter Type 1
BBXRT	1990-12-02		0.3-12	765	380	Wolter Type 1
CubeX	N/A	XIS	0.6-4	20	50	Mini Wolter Type 1
STROBE-X	N/A	XRCA	0.2-12	21760	300	Wolter Type 1
XPNAV-1	2016-11-10	TSXS	0.4-15	30	60	Wolter Type 1

This catalog provides a baseline to compare against mission concepts and inform what is possible or useful when designing a new device. Table 1 can be used to predict what range of scale is necessary to achieve the navigation goals based on similar existing X-ray technologies. Since smaller instrument scales must leverage new lensing mechanisms, extrapolating from the established trends is more theoretical, but shows a niche for instruments smaller than the CubeX X-ray Imaging Spectrometer that pass the tipping point of fitting a 3U form factor. Constraints on smaller instruments like material absorption and higher angle-of-incidence lensing are discussed in Chapter 4.

Employing the design of a scaled instrument like NICER has led to larger and smaller instrument configurations. The STROBE-X and CubeX missions are presenting instruments with direct heritage from NICER with increased and decreased scale,

respectively.[13][14] The standard X-ray lensing techniques and detector hardware are very established; Wolter Type 1 telescopes with charge-coupled devices or silicon drift detectors cover the majority of X-ray astronomy. Other strategies are less common, outdated or still experimental and are essentially not implemented. Wolter Type 1 concentrators in the 500-2000 cm^2 range of effective areas have been identified as the staple. Establishment-breaking optics could improve on many aspects of this concentrating design by removing the need to align reflective shells, thus achieving a more compact effective area to focal length ratio which will be enabling for a CubeSat scale instrument.

CHAPTER 3. X-RAY NAVIGATION PERFORMANCE COMPARISON

This portion of the research analyzed X-ray navigation instrument performance from theoretical models and compared the predictions with flight results from the NICER instrument onboard the International Space Station. Previous formulation of expected error is used to set an expected lower bound, drawing heavily from Sheikh et al. [15] Before comparing the instrument performance, this chapter details a navigation scheme using pulsar signals. There are two parts to the navigation scheme: turning the raw observations of X-ray emissions from pulsars into useful measurements and applying the navigation algorithm to the measurements to produce a position estimate.

3.1 Pulsar Description and Emission Characteristics

Pulsars are a kind of neutron star, compact objects that form after the collapse of stars which shed most of their mass in a supernova. The typical estimate for a pulsar's mass is around 1.4 solar masses condensed in size to diameters on the order of 10 kilometers. [10] Conservation of angular momentum causes the neutron star to spin rapidly as a neutron star collapses to such a small volume. The spinning magnetic field generates forces on the accretion disk and directs electromagnetic radiation along the poles of the magnetic field. When the magnetic poles and axis of rotation are not aligned, as depicted in Figure 4, the emission from the poles appears to flash like a lighthouse. The time dependent flux creates a unique pulse profile. The most useful pulsars fall in a category called millisecond pulsars which have periods between 0.001 and 0.05 seconds.

The raw X-ray observations from pulsars are very faint and require some signal processing to compile observations into one meta-observation.

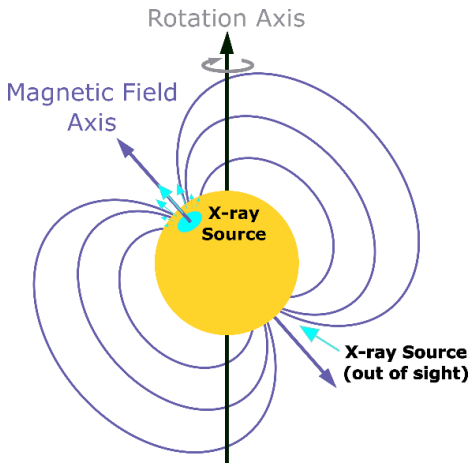

Figure 4 - Pulsar Axis Diagram

Pulsars emit periodic light curves, as seen in Figure 5. Individual pulse profiles are too faint to observe directly. The signal is stronger than the background and identifiable during occasional pulses but requires a signal processing strategy to produce useful measurements. Many pulses are averaged together by folding into time intervals spanning one pulse profile. This allows the periodic pulse to be discerned from background signals. Total background is a combination of emission from the target direction together with ambient noise caused by indirect transmission through the body of the instrument.

Of course, emission and rotation occur regularly at the pulsar's end, but the source is too faint to observe consistently by detectors thousands of parsecs away. By folding the observed particle counts over multiple oscillations, a stronger pulse profile

can be constructed.[16] Folding is a process of cutting the signal into one-period segments and ‘stacking’ to form an average signal. This is also called binning, as each time resolved portion of the period is bin of all photons with the same phase, modulo one period. The bins are created by dividing particles into segments of time, using the source period as determined from a reference catalog. In this way, integrating the signal over longer time intervals strengthens the Signal to Noise ratio of the average signal by creating one well-conditioned pulse profile. This measurement is used to determine a clear Time of Arrival of the pulse peak.

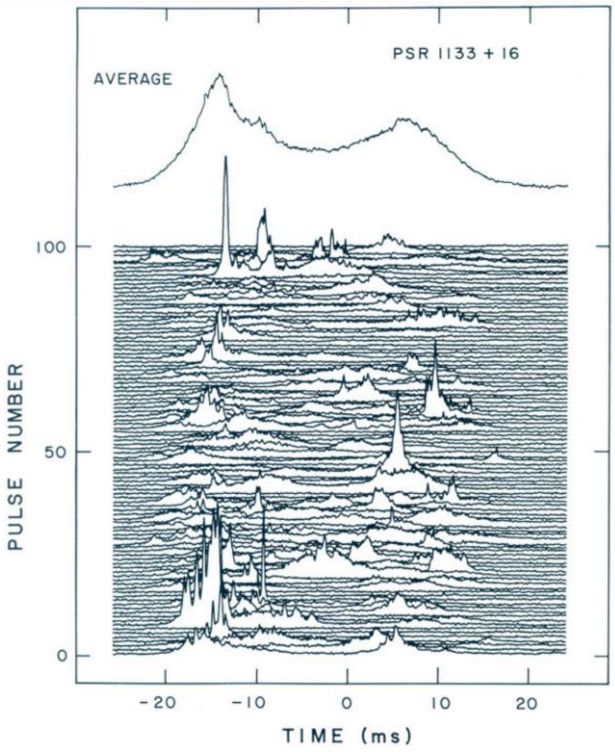

Figure 5 - Averaging Pulse Profiles Wrapped by Period [17]

Delta-correction Method

The current method for pulsar navigation is a procedure called Delta-correction that compares the observed time of arrival with an expected time of arrival computed from a reference catalog.[15] By taking the catalog epoch time of a leading-edge arrival and comparing it with an observed time of arrival, some time difference may be measured which is the phase offset of the arriving signal. The ToA difference represents a position offset calculated by the speed of light. This position offset is compared to the current state estimate to correct the position.

To compare observed and expected ToAs, these values are both converted to solar system barycenter which removes dependence on the position of Earth from catalog observations. There are many factors to consider when computing the expected ToA beyond just instrument position, including source period derivative, Doppler shift, relativistic effects, and line of sight. [18] The main factor of this conversion is the component of position offset along the line of sight vector to the target source. The SEXTANT team uses a standard utility from pulsar astronomy called Tempo2 which provides polynomials that describe the expected ToA with faster calculation speed than higher fidelity models also available from Tempo2. [19]

The pulses emitted cannot be individually identified or tied to a unique time of origination. Therefore, only the relative phase measurements from folded pulse profiles described previously are useful for navigation. This allows placement of one integrated pulse profile time of arrival within the span of one period. The integration periods are long, and it is crucial to propagate a state estimate for each photon arrival time to

properly compute a coherent pulse profile that accounts for spacecraft motion. The pulse periods are very short, as expected for sources called millisecond pulsars. Since the speed of light is high, one period spans 450 to 10,000 kilometers depending on the rotational velocity of the specific source. This window size represents the largest initial estimate error that can be correctly processed by the navigation algorithm. If an initial error is presented within this range or higher, the Delta-correction method may calculate the phase offset by an integer number of periods and produce dramatic range-estimate inaccuracies.

3.2 Analysis of SEXTANT Error

Pulsar navigation theory is not new, and several decades of publications exist supporting and investigating the subject.[16][17] The SNR form in equation 3, taken from [15] will serve as the token of previous theoretical calculations for comparison with SEXTANT experimental data. This resource is chosen by its author's involvement in other programs including references by the SEXTANT, STROBE-X and CubeX publications. Among other navigation products, Dilution of Precision error formulation is compared to data presented in Figure 6 by identifying the configurations of pulsars used during the portions of discrete error jumps. The specific navigation algorithm used for the SEXTANT demonstration was not obtained for this study, however raw NICER data and results from the work are published, along with comments on the team's algorithm development. Again, the HEASARC site was invaluable in providing direct access to the schedule of observation targets and durations. [20]

$$SNR = \frac{F_{pulsar}\, p_f\, A\, t_{obs}}{\sqrt{\left(B_X + F_{pulsar}(1 - p_f)\right) d\, A\, t_{obs} + F_{pulsar}\, p_f\, A\, t_{obs}}} \quad (3)$$

The Signal to Noise Ratio in Equation 3 is calculated using the counts of X-ray photon arrival events F_{pulsar} from the target source, and B_X from background radiation both with units of photons / (cm^2 s). The percentage of the total pulsar emission due to the pulsed portion is the "pulsed fraction," p_f. The duty cycle, $d = \frac{W}{P}$, is the ratio of the pulse width in seconds to the pulse period. Detector area and total observation time are A and t_{obs}. This form of Signal to Noise Ratio achieves $\sqrt{F_{pulsar}\, A\, t_{obs}}$ at best when the pulsed fraction is one and there is no background radiation. Signal is included in the denominator because the discrete arrival events are infrequent enough to be well represented by a Poisson distribution with rate parameter, which is variance, $\lambda = \sigma^2 = F_{pulsar}\, A\, t_{obs}$.

The SNR calculations from numeric examples provided by Sheikh were reproduced, so this formulation is consistent given some implicit assumptions, most notably flux and pulse profile characteristics from the 2-10 keV band. There are some nuances to the units, and the values from Appendix A were drawn primarily from table 3-2 in [21]. The flux and background rates should be unitless 'counts' of photons per unit area per unit time. In [15], energy flux rates in ergs/(cm^2 s) are presented, which can be converted to photon counts by looking at photons of a certain average energy, such as ~3.75keV/photon for the 2-10 keV band. [21] Ergs and electron-Volts are both units of energy and can be converted by equation 1.

The amount of observation time required to produce a specific SNR scales with instrument size. In the Signal to Noise Ratio analysis presented by Sheikh, observation time and detector area appear together and multiplied, so time and area can scale inversely and maintain the same accuracy. This is where the SNR formulation starts to show that it is more suited for describing instantaneous observability of a signal. In contrast, the presentation from equation 4 shows that the usefulness of n observations to discern a target flux scales with $\sqrt{n}$ when applying a period-modulated binning technique. [11]

$$F_{min} = \frac{S}{QA_s}\sqrt{\frac{B_i A_b + Q\Omega j_d A_s}{t\ \delta E}} \tag{4}$$

The goal of equation 4 is to calculate the minimum discernable flux for a given SNR of S, with F_{min} being S standard deviations above the mean background B. Total background is a combination of intrinsic detector background B_i and diffuse background $B_d = Q\Omega j_d$ where Q is the detector efficiency (counts per photon), Ω is the instrument aperture (steradians) and j_d is the diffuse flux (photons / (cm^2 s keV sr)). Instrument bandwidth is δE, geometric area collecting source and diffuse photons is A_s, geometric area for detector background is A_b. There are factors relevant to this problem that the token SNR calculation does not account for, including bandwidth which will be raised as a source of discrepancy later. Also, worth highlighting is the ratio of source directed area to background area, A_s / A_b, which provides signal gain.

The NICER instrument's capabilities are analyzed by using expected signal to noise to produce a variance for each X-ray source by equation 5 that is applied to weight

geometric dilution of precision. This discussion covers analysis of DoP predicted for the SEXTANT in-flight test from 2017 spanning days 313-316 of that year, from November 9th at 20:33:37 through November 11th. X-ray sources observed include J0218+4232, B1821-24, J0030+0451, and J0437-4715 as primary targets, with several miscellaneous targets mixed in. The SEXTANT three-sigma, reported error is many kilometers better than the predicted one-sigma lower bound on accuracy, as shown in Figure 6.

$$\sigma_{range} = c\frac{W}{2\,SNR} \tag{5}$$

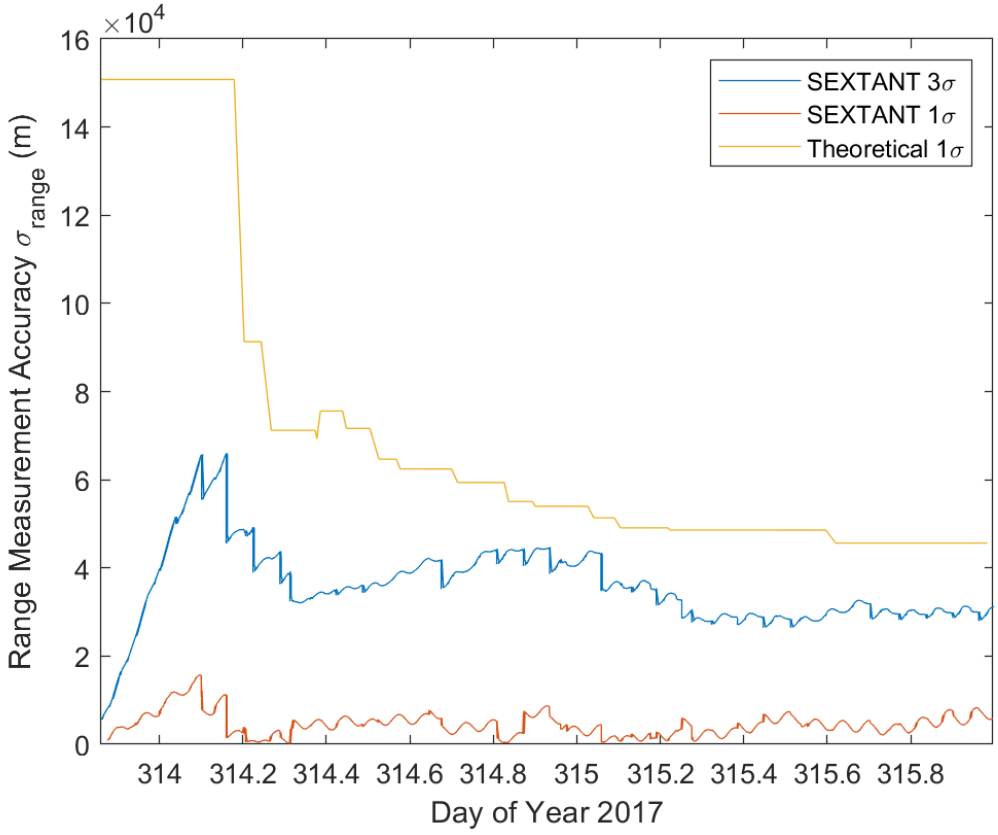

Figure 6 - Theoretical and Flight RSS Error

3.3 Sources of Analytical Discrepancy

Although the exact cause for the discrepancy in analytical and reported results on the accuracy of the NICER navigation solutions is not known, there are several possible explanations. Using the same hardware for catalog generation and navigation is one potential source of the discrepancy. The catalog of pulsar ToAs and pulse profiles used for the flight demonstration were augmented by several months of observation by NICER. Comparing arrival times with a rising edge established on the same hardware is liable to improve accuracy artificially by aligning signal artifacts generated by the hardware. In addition, the NICER instrument has high resolution timing of 100 nanoseconds and the benefits of binning with this level of precision are not by represented by the references, given in Appendix A. [18]

Another significant difference between the SNR formulation and the reported NICER results is the use of a navigation filter. The dilution of precision calculation has no selection or weighting to account for less reliable sources, and therefore presents degraded accuracies. For the flight demonstration, X-ray sources J0218+4232, B1821-24, J0030+0451, and J0437-4715 produced dilution of precision of 2838.1, 87.4, 54476.9 and 17506.3 meters, respectively after their total observation times. The total effective area assumed here was 1900 cm^2 with total observation times of 61478, 36593, 14891, and 2648 seconds. The last two pulsars have much lower pulsed fractions, much lower observation times, and significantly reduced accuracy. The result was an accuracy in Earth Centered Inertial frame of [41793.1, 11714.7, 14084.1] meters.

Two of the sources are well within the accuracy goal of 10 kilometers worst direction (17.3 km RSS) after the two-day demonstration. Worst direction describes the maximum component of the accuracy expressed in three dimensions applying the variance to the line of sight to each pulsar. The SEXTANT success criterion was to achieve this accuracy within two weeks of exposure to navigation sources. The SNR formulation does meet this criterion – giving three-dimensional accuracy of [9262.8, 1920.3, 1749.8] meters – assuming observation time is accumulated over the entire two weeks, split among the four targets at 302400 seconds each.

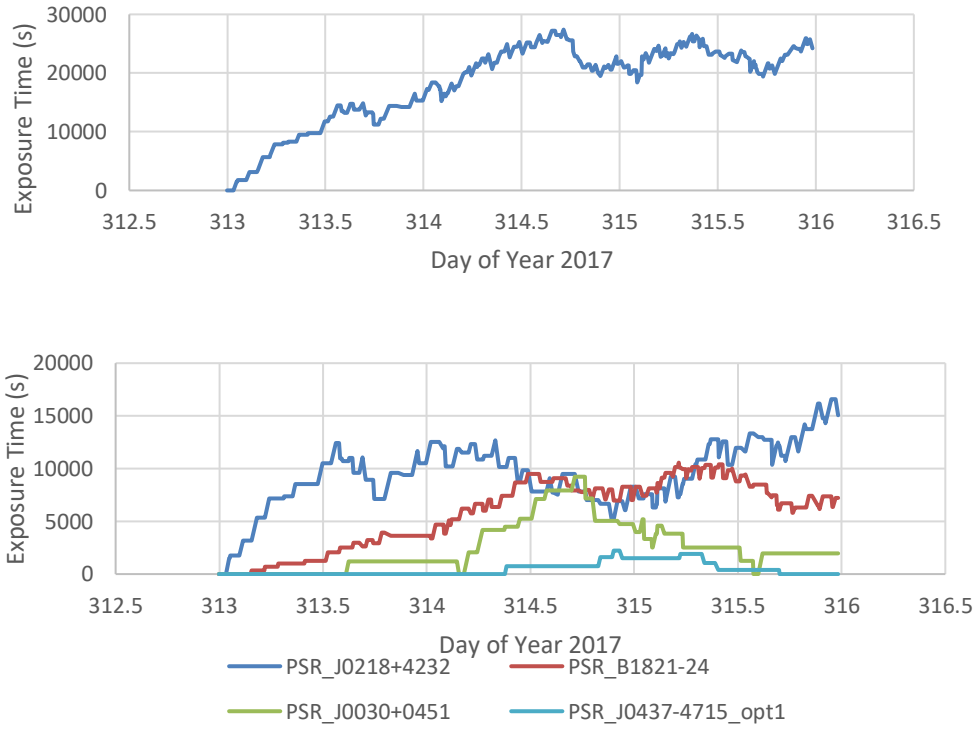

Figure 7 - (top) Total NICER Exposure Time to Primary SEXTANT Targets in a Rolling 0.55 Day Window (bottom) Exposure Time to each Individual Targets in the same Rolling Window

The range error predicted by SNR has several implicit assumptions that cause it to diverge from the observed error, but it does capture trends and features of the flight performance. Observation time is a key factor. The total instrument exposure time was not spread evenly across the targets and the rates of exposure accumulation varied. Figure 6 (bottom) shows the total exposure time changing over the course of the demonstration, building until the X-ray navigation estimate outweighs the propagated state, then remaining loosely level.

Another source of inaccuracy is a conservative assumption for background flux. To arrive at the same values as given in [15], the background flux is assumed to be constantly 3e-11 erg / (cm^2 s), or equivalently 0.005 photons / (cm^2 s) isotropic ambient irradiance from photons in the 2-10 keV band. This value is used as a conservative value meant to account for pulsar produced noise that is not well understood. To investigate the effects of the background term, flux was divided by 5 to a value of 0.001 photons / (cm^2 s), but the theoretical error was still more than 10 km higher than the experimental 1σ error. Therefore, this is not considered a major driver of discrepancy between the flight data and theoretical predictions.

The most disruptive source of inaccuracy is the flux range and pulse profile characteristics that depend on the energies observed. The theoretical calculation and Appendix A apply pulse profile characteristics observed over 2-10 keV, while the SEXTANT algorithm specifically describes using 0.2-8 keV and calls out 0.4-2 keV as 'critical'. The NICER instrument is sensitive to 0.3-12 keV. Most of these targets are brightest in a range near 0.2-1.5 keV, with similar emission to figure 5.9 from [22].

Flux and pulsed ratio exhibit energy dependent values. Pulse ratio is highest in the soft X-ray band 0.7-2 keV, although the magnitude of change with respect to energy varies from pulsar to pulsar. At lower energies, 0.1-0.7 keV, pulsars emit more ambient flux disproportionately with pulsed flux, causing higher photon counts but lower pulsed fraction.[23] The best observation window is 0.5-2 keV to maximize pulsed fraction with a reasonably large flux. Observing a larger energy band does not provide a benefit. The flux is increased, but the pulsed flux ratio is weakened. The change is variable by source and instrument and cannot be described conclusively with one example. To show the typical change observed, the flux (as a photon count per unit time) and pulsed fractions of PSR J1929+10 are 493 events with a pf = 0.36+/-0.11 for 0.5-5 keV, and 282 events with a pf = 0.69 +/- 0.18 for 0.5-2 keV. More observation is required, but it has been observed for many pulsars that SNR improves when energies from 0.3 through 2 keV are included in the measurement processing. This soft band is within NICER's detection spectrum. This presumably gives NICER better resolution of the pulse profile to provide greater phase alignment and therefore range correction accuracy.

The theoretical error can be reduced to match flight errors by increasing the pulsed flux fraction of J0030+0451 and J0437-4715 from 0.1 and 0.275 to 0.69 and 0.3 respectively. These new values are observationally determined for the range 0.1-2.4 keV.[24][25] This brings their pulse fractions roughly in line with the other two sources. This pulsed fraction is a meaningful reference for energies in this spectrum. Given that NICER is sensitive to energies as low as 0.2 keV, using predicted values from the soft X-ray spectrum is valid and necessary for estimation.

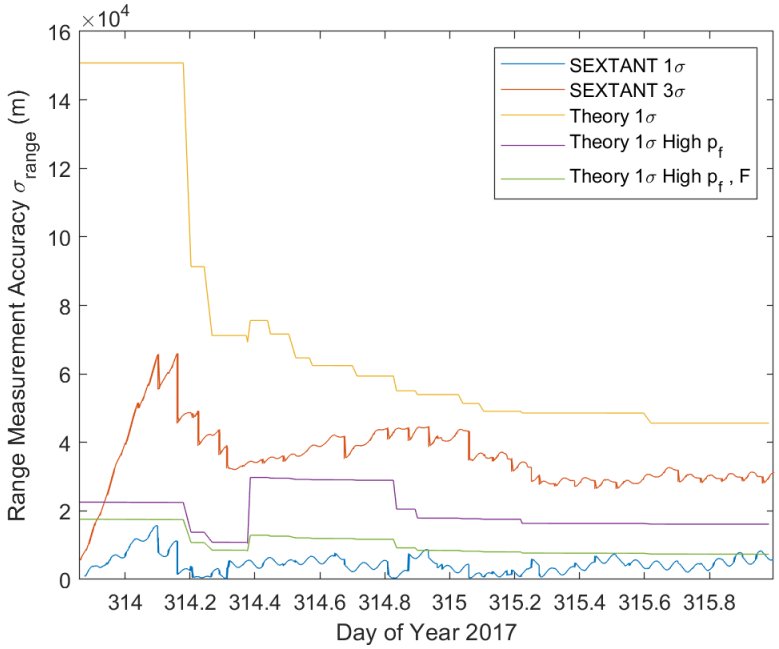

Figure 8 - Theoretical accuracy approaches experimental results with higher pulse fractions, which are observed at soft X-ray energies [0.2-2 keV]

As seen in Figure 8, position accuracy is sensitive to catalog pulse fraction and pulse width. Changing the pulsed fractions to the higher observed values brings the Theoretical 1σ error below the flight 3σ, demonstrated by "Theory 1σ High p_f" in Figure 8. Including the higher photon arrival count and pulsed-fraction from the softer energy band brings the theoretical even further in From the theoretical accuracy estimates, a change of pulse width from 4.6e-4 s to 5.7e-4 s produced 1.1 km vs 1.4 km error for J1715-305 which has a period of 0.0023 seconds. One millisecond of imprecision on pulse width (5% of the period) produces 26% range accuracy estimate error.

3.4 Performance of Navigation Instruments

Approximating a new instrument that is directly scaled from the NICER hardware, the SNR formulation can act as a guideline for performance. From comparison with the SEXTANT demonstration, the SNR into position accuracy provides a conservative estimate of the observation time and area required to produce useful navigation measurements.

The area of a CubeSat may seem miniscule compared to modern observatories since one face of a "1U" is not even capable of holding one of the 56 NICER XRCs, which have a 105 mm diameter. The effective area for each NICER concentrator is ~50 cm^2 at 1.5 keV, lower than geometric collecting area of 86.6 cm^2. Large telescopes cannot achieve real time observations. Reducing area does cost a significant amount of additional observation time to achieve 1 km accuracy. Figure 9 (a) shows the targets used for the SEXTANT demonstration with pulse fractions representing a wider soft X-ray band. Achieving 10-20 km accuracy is achieved in under 1 day, also demonstrated in Figure 8. To achieve better than 1 km accuracy theoretically takes over 100 days, but this is not realizable, since ToAs are compared to an expected ToA based on state estimate and state propagators will drift significantly while the navigating craft moves during the long exposure time. Figure 9 (b) shows the predicted accuracy for several targets using the original 2-10 keV band.

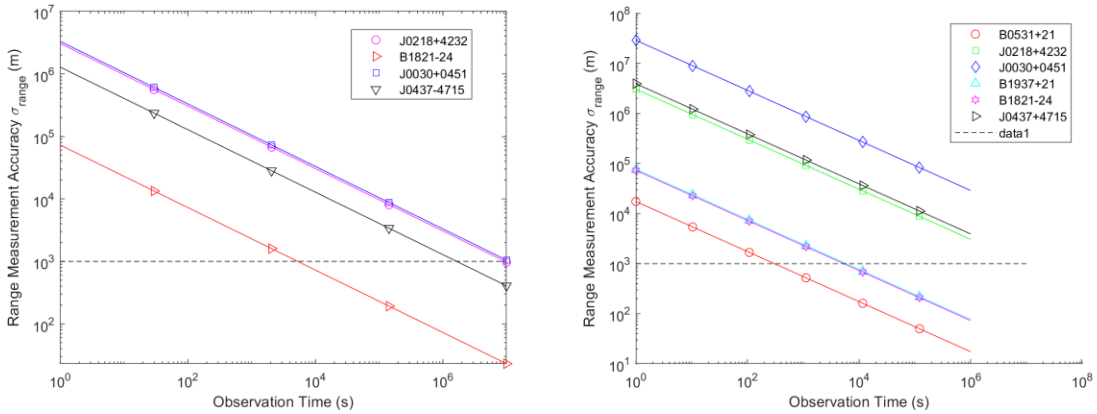

Figure 9 - (a) Range accuracy vs observation duration with 100 cm^2 detector [0.1-10 keV] for SEXTANT targets (b) Range accuracy vs observation duration with 100 cm^2 detector and X-ray background flux 0.005 photons/(cm^2 s) [2-10 keV]

An autonomous X-ray Delta-correction and state-estimate propagator is viable for interplanetary trajectories at a small scale. Relative to current navigation methods which rely on DSN tracking, the sensitivity required for pulsar observations is favorable and does not scale with distance from Earth. An X-ray instrument performs favorably compared to existing navigation strategies, which tend to gain accuracy around planetary bodies, but loose precision as the vehicle moves away from Earth-based references.

CHAPTER 4. X-RAY CONCENTRATOR INSTRUMENT CONCEPT FOR SMALL SATELLITES

After work on the demonstration comparison, results are promising for an X-ray pulsar navigation instrument. The NICER X-ray concentrator array, used to demonstrate X-ray navigation, performed better than the theoretical predictions by taking advantage of soft X-ray pulse profile features in the 0.3-4 keV band. However, NICER's XRCs are significantly out of scale for small satellite missions since its focal length is 1.085 m. [26] Many elements of the NICER design are still applicable to a CubeSat mission. Notably, the X-ray Timing Instrument comprises an array of Amptek FAST SDDs that are individually on an appropriate scale for the CubeSat form factor. The NICER instrument is shown in Figure 10 with a soccer ball for scale.

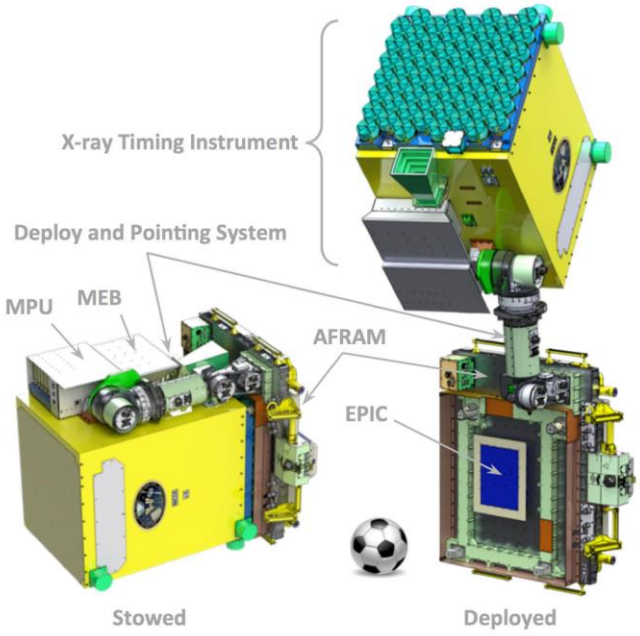

Figure 10 - NICER in its stowed and deployed configurations. [2]

Due to the repeating pattern of the detection optics, a subscale version could conceivably be constructed to detect X-ray emission at a scale that matches the needs of common small satellite platforms, which is the goal of the ongoing XPNAV-1 flight and CubeX mission proposal. The array on NICER was designed to study the interior composition of neutron stars and so the energy resolution and signal to noise ratio provided by the instrument yields more margin than a navigation application would require, where the primary metric is signal phase timing.

Focal length is one of the two major factors contributing to the scale of the NICER instrument. The majority of NICER's length is slightly more than one meter of empty space to accommodate the focal length between the X-ray concentrators and the photon detectors. The second factor contributing to instrument scale is the 2D collection area, which determines the photon reception counts and must be chosen to achieve a certain ratio above the background count to allow meaningful measurements to be made, per equation 4. Mission designs using small-scale traditional Wolter Type 1 concentrators to view pulsars – such as the XACT sounding rocket, the XPNAV-1 satellite, or the CubeX proposal – report collection areas bellow 100 cm^2 as capable of detecting pulsars, which means a 1U face presents a sufficient collector area. [27][28][14] The focal lengths of these small instruments are still longer than 50 cm. While larger collection area is convenient and reduces observation time, the XPNAV-1 satellite presents flight data showing its 30 cm^2 geometric area with the gain of a Wolter Type 1 telescope can detect the Crab Pulsar with photon count rate scaled linearly with area compared with NICER results.[28]

4.1 Instrument Design

A study of components and fabrication techniques to create an X-ray navigation instrument of appropriate size and mass for a 3 or 6U CubeSat is presented to identify concepts for physical testing. The objective of this design is maximizing both the effective area of an instrument for soft X-rays 0.3-4 keV and the ratio of directed area to diffuse background area, A_s / A_b. The background area is defined by the exposed detector area. The NICER XTI uses Amptek FAST SDD detectors with a 70 mm^2 detector area and a reduced window of 2 mm^2. Using this detector, the remaining discussion describes concentrator configurations that attempt to achieve a focal length suitable for a 3U CubeSat form factor.

Compound refractive lenses were demonstrated for X-rays in 1996 and have shown promise for reducing X-ray focal length to a scale applicable to CubeSats.[8] CRL configurations provide a focal length reduction by more than a factor of 10 over standard Wolter Type 1 optics.

CRL lenses shorten focal lengths enough to fit a concentrator and detector within 3U volumes. Lenses from 2 to 4 cm can focus X-rays in 4 to 11 cm to support the desired instrument.[29] However, they are hampered by absorption within the lensing material, and are less effective at soft energies below 5 keV. CRL configurations have been studied for focusing beam lines of small initial area, on the order of square millimeters. Arrays of CRL columns have been produced in a fashion that scales the effective area to compete with larger two-dimensional lenses. Several adaptations of CRL arrays have been

presented over the last two decades which show improving results for the future of a soft X-ray concentrator with shortened focal length.

A promising evolution of the CRL design is a saw-toothed lens, pictured in Figure 11 (left). [30] Like CRLs, sawtooth lenses were not designed with spacecraft in mind, but are proposed in other works – notably [7],[8] and [301] – for X-ray microscopes and spectroscopy to consolidate lab space and make some X-ray beam-line applications more practical. Sawtooth or Multi Prism Lenses (MPLs) have less material along the centerline of transmission, so they achieve higher efficiencies by reducing material attenuation compared to standard CRL configurations. Sawtooth lenses concentrate photons by presenting several prisms that project the shape of a concave lens. This style is also easier to manufacture, since it has linear features. MPLs have produced focal lengths shorter than 30 centimeters, but they only focus in one dimension. This produces a line of focus, instead of a focal point, which is not useful for the circular target of the detector. Two layers of MPL lenses with orthogonal focusing axis can be used to create an array of focal points, but this strategy can only space the focal points out by the distance between lenses. For a volume constrained application, the lenses would be as closely packed as possible and the distance between focal points would be on a micrometer scale, which precludes the use of an array of detectors at each focal point. [31]

Figure 11 - (left) Sawtooth CRL (center) Assembled Stack of SPLs (right) One Element of the SPL Assembly [32]

A recent strategy for two-dimensional lensing was presented using a "Stacked Prism Lens" which applies the useful features of CRL arrays to a radially symmetric configuration.[32] Using a N=10 layered stack of lenses tuned for hard X-rays achieves a focal length of 10.9 cm and an effective area of 27 cm^2 at 10 keV. The focal length, f, will shorten for soft X-rays per equation 6 as decrement of index of refraction, δ, grows to approximately 10^{-3} for a constant radius of lens curvature, R. The effective area will also decrease as the energy goes off-design, with a lower limit on design-energy based on manufacturability. A hard X-ray lens has a smallest length component of 47 micrometers, compared to 3 micrometers at 1 keV.

$$f = R/2N\delta \tag{6}$$

Material selection affects the real part of index of refraction, $n_r = 1-\delta$, where the decrement is described by equation 7, where λ is wavelength, ρ is density in g / cm^3, Z is atomic number and A is atomic mass. This means larger atomic numbers achieve shorter focal lengths at the same radius of curvature. Importantly, lower atomic number also means lower mass absorption coefficient $\frac{\mu}{\rho} \cong Z^3/E^3$ for some attenuation coefficient, μ. Material attenuation is stronger at lower energies and so low atomic number materials like Lithium and Beryllium are top choices.

$$\delta = 2.70\left(\frac{\lambda^2 \rho Z}{A}\right) \times 10^{-6} \tag{7}$$

Fabrication of SPLs has been demonstrated using SU-8, a UV photoresistive material. Previous CRL demonstrations have promoted Poly(methyl methacrylate), PMMA, which has low material attenuation. [33] However, PMMA, SU-8 and other plastics are not suited for space applications since they outgas and have a high affinity for water. Beryllium is a better choice for this application, since it has a very low atomic number and high melting point.

Some progress has been made towards suitable lenses compact form-factors. To focus soft X-rays with SPL type optics requires even more precise fabrication techniques to accurately produce features at a 1-micron scale. Additional consideration should be taken to attempt to create the lens disks using beryllium to reduce material absorption for effective soft X-ray lensing, although aluminum if sufficient for prototyping and developing fabrication techniques. If scale and material processing can be resolved, then SPL configuration optics will enable small-satellite autonomous pulsar navigation.

CHAPTER 5. CONCLUSION

The goal of this work is to contribute to development of a small-scale autonomous X-ray position estimating instrument for small satellite missions. The primary contribution is the analysis of theoretical X-ray navigation performance compared to recent flight results from the NICER instrument. Experimental validation of the theory was achieved after adjusting the source catalog to include a softer energy band from 0.3-4 keV. The NICER instrument is tuned for maximum effective area in this band, and the theoretical accuracy more closely matched the observed range errors after the catalog was adjusted to include pulsar characteristics from the soft band. Pulsar emissions in the soft X-ray band have higher ambient flux and pulsed flux fractions, which significantly improves range measurements.

Further exploration of small-scale soft X-ray navigation instruments is required, but there has been promising development over the past decade. The crucial requirement for new instruments is sensitivity to the soft X-ray band 0.3-4 keV. As a starting point, milestone X-ray observatories are cataloged to define the modern design space. Current experimental lensing configurations are discussed to highlight the technical challenges of creating a novel instrument. Recent developments in Stacked Prism Lenses are promising for CubeSat form factors. Additional studies are required to develop fabrication methods using Beryllium to be sensitive to the X-rays in the 0.3-4 keV band, identified as useful in Chapter 3. By documenting the state-of-the-art, this work hopes to provide a resource to benchmark future projects against, allowing for faster development by providing an accessible summary of existing technology.

APPENDIX A. X-RAY SOURCE CATALOG

```
%% CATALOG
%crab pulsar
%RA = 05h 34m 33.22s
%Declination = 22° 00' 52.86"
xrs.name = 'B0531+21';
xrs.ra = 1.4596;
xrs.dec = 0.3842;
xrs.p = 0.0335045369458; %seconds Period
xrs.f_xray = 1.54; %photons/(cm^2 s) [2-10 keV]
xrs.pulsed_frac = 0.7;
xrs.w = 0.00167; %seconds Pulse width (FWHM)
catalog = [catalog,xrs];

% 'B1937+21'
ra = 5.1356;
dec = 0.3665;
p = 0.00156; %seconds Period
f_xray = 4.99e-5; %photons/(cm^2 s) [2-10 keV]
pulsed_frac = 0.86;
w = 0.000021; %seconds Pulse width (FWHM)

% 'B1821-24'
ra = 4.8040;
dec = -0.4188;
p = 0.00305; %seconds Period
f_xray = 1.93e-4; %photons/(cm^2 s) [2-10 keV]
pulsed_frac = 0.98;
w = 0.000055; %seconds Pulse width (FWHM)

% 'J0218+4232'
ra = 0.6021;
dec = 0.7423;
p = 0.00232; %seconds Period
f_xray = 6.65e-05; %photons/(cm^2 s) [2-10 keV]
pulsed_frac = 0.73;
w = 0.00035; %seconds Pulse width (FWHM)

% 'J0030+0451'
ra = 0.1308;
dec = 0.0846;
p = 0.00487; %seconds Period
f_xray = 1.96e-5; %photons/(cm^2 s) [2-10 keV]
      %f_xray = 2.35e-5; [0.1-2.4 keV]
pulsed_frac = 0.1; % *** 0.69 [0.1-2.4 keV] ***
w = 0.00024; %seconds Pulse width (FWHM)
```

```
% 'J0437-4715'
ra = 1.2086;
dec = -0.8246;
p = 0.00575; %seconds Period
f_xray = 6.65e-5; %photons/(cm^2 s) [2-10 keV]
     %f_xray = 2.35e-5; [0.1-2.4 keV]
pulsed_frac = 0.275; % *** 0.3 [0.1-2.4 keV] ***
w = 0.00029; %seconds Pulse width (FWHM)

% 'XTE J1751-305'
ra = 4.6731;
dec = 0.5344;
p = 0.0023; %seconds Period
f_xray = 0.181; %photons/(cm^2 s) [2-10 keV]
pulsed_frac = 0.055;
%w = 0.00046; %seconds Pulse width (FWHM)
w = 5.7e-4;

% 'J1012+5307'
ra = 2.6703;
dec = 0.9270;
p = 0.00526; %seconds Period
f_xray = 1.93e-6; %photons/(cm^2 s) [2-10 keV]
pulsed_frac = 0.75;
w = 0.00026; %seconds Pulse width (FWHM)

% 'J2124-3358'
ra = 5.6025;
dec = -0.5928;
p = 0.00493; %seconds Period
f_xray = 1.28e-5; %photons/(cm^2 s) [2-10 keV]
pulsed_frac = 0.282;
w = 0.00025; %seconds Pulse width (FWHM)

% 'J2214+3000'
% source: https://www.osti.gov/pages/servlets/purl/1357271
ra = 5.8234;
dec = 0.5237;
p = 0.003119226579079; %seconds Period

% 'J0751+1807'
ra = 2.0551;
dec = 0.3161;
p = 0.00347; %seconds Period
f_xray = 6.63e-06; %photons/(cm^2 s) [2-10 keV]
pulsed_frac = 0.70;
w = 0.00017; %seconds Pulse width (FWHM) *estimated*
```

```
% 'J1024-0719'
ra = 2.7227;
dec = -0.1276;
p = 0.00516; %seconds Period
f_xray = 1.37e-06; %photons/(cm^2 s) [2-10 keV]

% 'B1957+20'
ra = 5.2228;
dec = 0.3490;
p = 0.0016; %seconds Period
f_xray = 8.31e-5; %photons/(cm^2 s) [2-10 keV]
pulsed_frac = 0.6;
w = 0.00008; %seconds Pulse width (FWHM) *estimated*

% 'B0540-69'
ra = 1.4835;
dec = -1.2042;
p = 0.05037; %seconds Period
f_xray = 5.15e-03; %photons/(cm^2 s) [2-10 keV]
pulsed_frac = 0.67;
w = 0.0025; %seconds Pulse width (FWHM) *estimated*
```

REFERENCES

[1] Hewish, A., Bell, S. J., Pilkington, J. D., Scott, P. F., and Collins, R. A., "Observation of a Rapidly Pulsating Radio Source," Nature, Vol. 217, 1968, pp. 709-713.

[2] Keith C. Gendreau, Zaven Arzoumanian, Phillip W. Adkins, …, "The Neutron star Interior Composition Explorer (NICER): design and development", 9905, 2016, doi=10.1117/12.2231304, https://doi.org/10.1117/12.2231304

[3] Mitchell, J. W., Winternitz, L. B., Hassouneh, M. A., Price, S. R., Semper, S. R., Yu, W. H., . . . (2018). "SEXTANT X-ray Pulsar Navigation Demonstration: Initial On-Orbit Results." AAS 18-155, GSFC-E-DAA-TN51842

[4] T.J. Martin-Mur, E.D. Gustafson, B.T. Young, "Interplanetary Cubesat Navigational Challenges", 25th Internatonal Symposium on Space Flight Dynamics, 2015.

[5] "CubeSat Design Specification", revision 13, the CubeSat Program, Cal Poly San Luis Obispo, February 2014.

[6] Jet Propulsion Laboratory, "Deep Space Network: Current Mission Set", https://deepspace.jpl.nasa.gov/about/commitments-office/current-mission-set/ (Accessed July 30, 2019)

[7] N. Kokareva, A. Petrov, V. Bessonov, … "Fabrication of 3D x-ray compound refractive lenses by two-photon polymerization lithography (Conference Presentation)," Proc. SPIE 10675, 3D Printed Optics and Additive Photonic Manufacturing, 106750E (29 May 2018)

[8] Snigirev, V. Kohn, I. Snigireva, and B. Lengeler, "A compound refractive lens for focusing high-energy X-rays" Nature (London) 384, 49 (1996).

[9] Office of Radiological Safety, "Radiation Safety Policy Manual", https://www.ehs.gatech.edu/radiation/xray (Accessed May 14, 2019)

[10] https://www.astro.umd.edu/~richard/ASTR480/xray-telescopes.pdf Encyclopedia of Astronomy and Astrophysics, Nature Publishing Group (2001)

[11] Fraser, G. W., *X-Ray Detectors In Astronomy*, Cambridge Univ. Press, Cambridge, England, U.K., 1989.

[12] JAXA (2016) "Hitomi Anomaly Report", https://global.jaxa.jp/projects/sat/astro_h/files/topics_20160524.pdf

[13] Ray, Paul S., et al. "STROBE-X: a probe-class mission for x-ray spectroscopy and timing on timescales from microseconds to years." 10699, SPIE Astronomical Telescopes + Instrumentation, 2018, https://doi.org/10.1117/12.2312257, DOI 10.1117/12.2312257

[14] Stupl, Jan, et al. "CubeX: A Compact X-Ray Telescope Enables Both X-Ray Fluorescence Imaging Spectroscopy and Pulsar Timing Based Navigation." 32nd Annual AIAA/USU Conference on Small Satellites, 4 Aug. 2018, ntrs.nasa.gov/archive/nasa/casi.ntrs.nasa.gov/20180006866.pdf

[15] Sheikh, Suneel I., et al. "Spacecraft Navigation and Timing Using X-Ray Pulsars." Navigation, vol. 58, no. 2, 2011, pp. 165–186., doi:10.1002/j.2161-4296.2011.tb01799.x.

[16] Lorimer, D. R., Kramer, M., "Handbook of Pulsar Astronomy", Cambridge, Univ. Press, Cambridge, England, U.K., 2005.

[17] Craft, H. D., “Radio Observations of the Pulse Profiles and Dispersion Measures of Twelve Pulsars”, CORNELL UNIVERSITY, 1970, Dissertation Abstracts International, Volume: 31-09, Section: B, page: 5140.
[18] SEXTANT Algorithm Development, GSFC_12961_TN19695-1.pdf
[19] XNAV for Deep Space Navigation, Graven 2008, AAS 08-054
[20] Myers, J. D., (Accessed October 29, 2019), “Multi-Mission As-Flown Timeline Tool”, https://heasarc.gsfc.nasa.gov/cgi-bin/Tools/timeline/timeline.pl?mission=NICER
[21] Sheikh, S. I., “The Use Of Variable Celestial X-Ray Sources For Spacecraft Navigation,” Dissertation at the University of Maryland, 2005
[22] Slowikowska, A. “Pulsar Characteristics Across The Energy Spectrum,” Dissertation at the Nicolaus Copernicus Astronomical Center Department of Astrophysics in Torun, 2006
[23] Mineo, T., Cusumano, G., Kuiper, L., Hermsen, W., Massaro, E., Becker, W., “The pulse shape and spectrum of the millisecond pulsar PSR J0218+4232 in the energy band 1-10 keV observed with BeppoSAX”, Astronomy and Astrophysics, v.355, p.1053-1059 (2000)
[24] Becker, W., Trümper, J., “X-Rays from the Nearby Solitary Millisecond Pulsar PSR J0030+0451: The Final ROSAT Observations” The Astrophysical Journal, 545:1015-1019, 2000
[25] Pavlov, G. G., Zavlin, V. E., “Mass-to-Radius Ratio for the Millisecond Pulsar J0437-4715” Max-Planck-Institut für Extraterrestrische Physik, D-85740 Garching, Germany; 1997 October 23
[26] Okajima, T., Soong, Y., “Performance of NICER flight x-ray concentrator”, Proceedings of the SPIE, Volume 9905, id. 99054X 7 pp. (2016).
[27] Balsamo, E., Gendreau, K., “Development of full shell foil x-ray mirrors.pdf, NICER and XACT XRCs”, Proceedings of SPIE, Volume 8450, id. 845052 (2012)
[28] Kramer, Herbert J. “XPNAV-1 (X-Ray Pulsar Navigation Satellite-1).” Earth Observation Portal, 2019, eoportal.org/web/eoportal/satellite-missions/pag-filter/-/article/xpnav-1-x-ray-pulsar-navigation-satellite-1-#mission-status.
[29] Pina, L., Dudchik, Y., “X-ray imaging with compound refractive lens and microfocus x-ray tube”
[30] Cederström, B., Cahn, R., Danielsson, M. et al. “Focusing hard X-rays with old LPs”. Nature 404, 951 (2000) doi:10.1038/35010190
[31] J. Xu et al 2018 JINST 13 C07005
[32] Mi, W., “A Stacked Prism Lens Concept for Next-Generation Hard X-Ray Telescopes”, Dissertation at the KTH Royal Institute of Technology, Sweden 2019
[33] Lengeler, B., “Refractive X-Ray Lenses New Developments,” Physics Department RWTH Aachen University, Grenoble, 2010.
[34] Myers, J. D., (2019) “High Energy Astrophysics Observatories” https://heasarc.gsfc.nasa.gov/docs/observatories.html
[35] NASA, (2005), “AXAF Calibration: Wolter Telescope” https://commons.wikimedia.org/wiki/File:Wolter-telescope.gif

[36] Myers, J. D., (2019), “The Nuclear Spectroscopic Telescope Array Mission – NuSTAR”, https://heasarc.gsfc.nasa.gov/docs/nustar/

[37] K. S. Wood, M. Kowalski, M.N.Lovellette, P. S. Ray, M. T. Wolff, DJ. Yentis, E. O. Hulburt “The Unconventional Stellar Aspect Experiment on ARGOS” Center for Space Research, Naval Research Laboratory, AIAA 2001-4664